

# General relativistic magnetohydrodynamics simulations of prompt-collapse neutron star mergers: The absence of jets

Milton Ruiz<sup>1</sup> and Stuart L. Shapiro<sup>1,2</sup>

<sup>1</sup>*Department of Physics, University of Illinois at Urbana-Champaign, Urbana, IL 61801*

<sup>2</sup>*Department of Astronomy & NCSA, University of Illinois at Urbana-Champaign, Urbana, IL 61801*

Inspiraling and merging binary neutron stars are not only important source of gravitational waves, but also promising candidates for coincident electromagnetic counterparts. These systems are thought to be progenitors of short gamma-ray bursts (sGRBs). We have shown previously that binary neutron star mergers that undergo *delayed* collapse to a black hole surrounded by a *weighty* magnetized accretion disk can drive magnetically-powered jets. We now perform magnetohydrodynamic simulations in full general relativity of binary neutron stars mergers that undergo *prompt* collapse to explore the possibility of jet formation from black hole-*light* accretion disk remnants. We find that after  $t - t_{\text{BH}} \sim 26(M_{\text{NS}}/1.8M_{\odot})\text{ms}$  [ $M_{\text{NS}}$  is the ADM mass] following prompt black hole formation, there is no evidence of mass outflow or magnetic field collimation. The rapid formation of the black hole following merger prevents magnetic energy from approaching force-free values above the magnetic poles, which is required for the launching of a jet by the usual Blandford–Znajek mechanism. Detection of gravitational waves in coincidence with sGRBs may provide constraints on the nuclear equation of state (EOS): the fate of an NSNS merger—delayed or prompt collapse, and hence the appearance or nonappearance of an sGRB—depends on a critical value of the total mass of the binary, and this value is sensitive to the EOS.

PACS numbers: 04.25.D-, 04.25.dg, 47.75.+f

## I. INTRODUCTION

The LIGO collaboration has reported the direct detection of gravitational waves (GWs) from the inspiral and merger of at least three binary black hole (BHBH) systems [1–4]. Thus, it may be just a matter of time before GWs from merging black hole-neutron star (BHNS) and/or binary neutron stars (NSNS) systems are detected as well. Estimates from population synthesis and the current sensitive volume of the advance LIGO interferometers predict detection rates of  $\lesssim 4$  events per year for BHNS systems, and  $\lesssim 20$  events per year for NSNS systems (see e.g. [5–8]).

Merging BHNSs and NSNSs are not only important sources of gravitational radiation, but also promising candidates for coincident electromagnetic (EM) counterparts. These systems have long been thought to be the progenitors of *short* gamma-ray bursts (sGRBs) [9–19], which is strongly supported by the *first* detection of a kilonova associated with the sGRB “GRB 130603B” [20, 21].

Coincident detection of GWs with EM signals from compact binary mergers containing NSs could give new insight into their sources: GWs are sensitive to the density profile of NSs and their measurement enforces tight constraints on the equation of state (EOS) of NSs [22]. Post-merger EM signatures, on the other hand, can help to explain, for example, the phenomenology of sGRBs, and the role of these BHNS and NSNS mergers in triggering the nucleosynthesis processes in their ejecta (e.g., the r-process; see [23–25]).

Recently, self-consistent simulations in full general relativistic magnetohydrodynamics (GRMHD) of merging BHNSs [26] and merging NSNSs [27] that undergo *delayed* collapse have shown that when the NSs are suitably magnetized, a collimated, mildly relativistic outflow—an incipient jet can be launched from the spinning BH remnant surrounded by a highly magnetized accretion disk. In the BHNS sce-

nario, the key ingredient for jet launching is the existence of a strong poloidal B-field component after disruption [28, 29]. This property can be achieved if initially the NS is endowed with a dipole B-field that extends from the NS interior into a pulsar-like exterior magnetosphere. Following disruption, magnetic winding and the magnetorotational instability (MRI) build up enough magnetic pressure above the BH poles to allow the system to launch a jet after  $\sim 100(M_{\text{NS}}/1.4M_{\odot})\text{ms}$  following the BHNS merger [26]. The burst duration and the outgoing Poynting luminosity were found to be  $\Delta t \sim 0.5(M_{\text{NS}}/1.4M_{\odot})\text{s}$  and  $L_{\text{EM}} \sim 10^{51}\text{erg s}^{-1}$ , respectively, consistent with the observed duration of sGRBs and their corresponding luminosities [30]<sup>1</sup>. In the NSNS scenario, by contrast, jets arise whether or not the B-field is confined to the NS interior [27]. The key ingredient for jet launching seems to be B-field amplification due both to the Kelvin-Helmholtz instability (KHI) and to the MRI, which can boost the rms value of the B-field to  $\gtrsim 10^{15.5}\text{G}$  [31, 32]. The calculations in [27] showed that binary NSNSs that start from the late inspiral and undergo *delayed* collapse to a BH launch jets after  $\sim 44(M_{\text{NS}}/1.8M_{\odot})\text{ms}$  following the NSNS merger. The burst duration and its EM luminosity were found to be  $\Delta t \sim 97(M_{\text{NS}}/1.8M_{\odot})\text{ms}$  and  $L_{\text{EM}} \sim 10^{51}\text{erg s}^{-1}$ , respectively, also consistent with short sGRBs; see e.g. [33].

Although the above results were obtained using a simple,  $\Gamma$ -law EOS, it is expected that a realistic EOS will yield a similar outcome. Different EOSs affect the amount and composition of the ejecta during NSNS coalescences [34–39], and therefore, the ram pressure produced by the fall-back debris, as well as the mass of the accretion disk. The delay time for jet launching following the merger may therefore depend on the EOS. Moreover different EOSs have different threshold

<sup>1</sup> See e.g. <https://swift.gsfc.nasa.gov/archive/grb-table/fullview>

masses above which the collapse is prompt vs. delayed [40–42]. However, for all EOSs the most significant feature that determines whether jets can be launched is likely whether the merger remnant undergoes delayed or prompt collapse, although even in the delayed collapse, different EOSs have strong impact on the accretion disk [43, 44], and hence in the jet’s lifetime. The above result seems to be the main reason why in the much higher resolution but shorter NSNS simulations reported in [31], in which a H4-EOS is assumed and the B-field is confined to the NS interior, neither a magnetically driven outflow or a B-field collimation were observed. After  $t \sim 26\text{ms}$  following the BH formation, fall-back material in the atmosphere persisted. It is likely then that, at that point in the evolution, the ram pressure is still larger than the magnetic pressure and thus a longer simulation is required for the jet to emerge. While in the NSNS simulations reported in [45], in which the effects of different EOSs, different mass ratios, and different B-field orientations were studied, there is no evidence of an outflow or a jet, there is a formation of an organized B-field structure above the BH. Therefore, we expect that, in a longer simulation, a jet may be launched. See also [36] for a detailed discussion of the rotation profiles, the accretion disk evolution and amplification of the B-field, as well as the ejection of matter in magnetized merging NSNSs. Note also that neutrino pair annihilation alone may not be strong enough to power jets [46, 47].

To complete our preliminary survey of NSNS mergers as possible sGRB progenitors, we now consider magnetized NSNS configurations that lead to *prompt* collapse following merger. These events produce less massive accretion disks than those arising from delayed collapse (see e.g. [41, 43, 44]). For comparison purposes, we again consider NSNS binaries described initially by irrotational  $\Gamma = 2$  polytropes endowed with the same two B-field configurations employed in [27].

We find, in agreement with previous studies [41, 43, 44, 48, 49], that prompt collapse leads to a highly spinning BH remnant ( $a/M_{BH} \gtrsim 0.8$ ), with an accretion disk mass much smaller than  $0.01M_{\odot}(k/262.7\text{km}^2)^{1/2}$ , and increasing with greater disparity between the rest masses of the two NSs. Here  $k$  is the polytropic gas constant:  $k = P/\rho_0^{\Gamma}$ . Thus, these results are not altered by the presence of weak interior B-fields. We now also find that, in contrast to delayed collapse, the absence of a hypermassive neutron star (HMNS) epoch does not allow the magnetic energy to reach equipartition and, ultimately, force-free levels [32], thereby preventing B-field collimation along the remnant BH poles and an associated jet outflow.

Although our study is far from exhaustive, we tentatively conclude that GWs from merging NSNSs may be accompanied by sGRBs in the case of delayed collapse but not in the case of prompt collapse. This finding has important consequences. The fate of a NSNS merger – prompt or delayed collapse – is determined by a critical value of the total mass, and this value depends on the EOS [42, 50]. If the masses of the NSs in the binary can be reliably determined from measurements of the GWs during the pre-merger inspiral phase [51, 52], then the absence or presence of a counterpart sGRB following merger will shed light on the EOS.

This information may supplement other estimates of stellar radii and compactness from tidal imprints in the waveforms [53, 54]. Additionally, measurement of the time delay between the peak GW and sGRB signals may help provide an estimate of the initial NS B-field strength [55].

The paper is organized as follows. A short summary of the numerical methods and their implementation is presented in Sec. II A. A detailed description of the adopted initial data and the grid structure used for solving the GRMHD equations are given in Sec. II B and Sec. II C, respectively. Sec. II D contains the diagnostics employed to monitor our numerical calculations. We present our results in Sec. III. Finally, we offer conclusions in Sec. IV. We adopt geometrized units ( $G = c = 1$ ) throughout the paper, unless otherwise specified.

## II. NUMERICAL METHODS

### A. Numerical setup

We use the Illinois GRMHD code, which is embedded in the `Cactus`<sup>2</sup> infrastructure and uses `Carpet`<sup>3</sup> for moving mesh refinement. This code has been thoroughly tested and used in the past in numerous scenarios involving compact objects, including magnetized BHNS and NSNS simulations (see e.g. [26, 27, 56, 57]). A detailed description of the numerical methods, their implementation, and code tests can be found in, e.g., [57–59].

**Spacetime evolution:** We decompose the metric into 3 + 1 form,

$$ds^2 = -\alpha^2 dt^2 + \gamma_{ij} (dx^i + \beta^i dt) (dx^j + \beta^j dt), \quad (1)$$

with  $\alpha$  and  $\beta^i$  the familiar gauge variables and  $\gamma_{ij}$  the spatial metric induced on a spatial hypersurface with a future-directed, timelike unit vector  $n^{\mu} = (1/\alpha, -\beta^i/\alpha)$ . The full spacetime metric  $g_{\mu\nu}$  is related to the spatial metric by  $\gamma_{\mu\nu} = g_{\mu\nu} + n_{\mu}n_{\nu}$ . Associated with the time slice, we define the extrinsic curvature  $K_{\mu\nu} \equiv -\gamma_{\mu\alpha}\nabla^{\alpha}n_{\nu}$ . Geometric variables are then evolved via the Baumgarte–Shapiro–Shibata–Nakamura (BSSN) formulation [60, 61]. The resulting evolved variables are then the conformal exponent  $\phi = \ln(\gamma)/12$ , conformal metric  $\tilde{\gamma}_{ij} = e^{-4\phi}\gamma_{ij}$ , the trace of the extrinsic curvature  $K$ , the conformal trace-free extrinsic curvature  $\tilde{A}_{ij} = e^{-4\phi}(K_{ij} - \gamma_{ij}K/3)$  and the three auxiliary variables  $\tilde{\Gamma}^i = -\partial_j\tilde{\gamma}^{ij}$ . We evolve these variables using the equations of motion (9)–(13) in [56]. We close the system of equations of motion in the geometric sector by using 1+log time slicing and the gamma-driver spatial shift conditions [62, 63] cast in first order form (see e.g. [64]). For numerical stability, we set the damping parameter  $\eta$  appearing in the shift condition to  $\eta = 0.85/M$ , with  $M$  the ADM mass of the system.

<sup>2</sup> <http://www.cactuscode.org>

<sup>3</sup> <http://www.carpetcode.org>

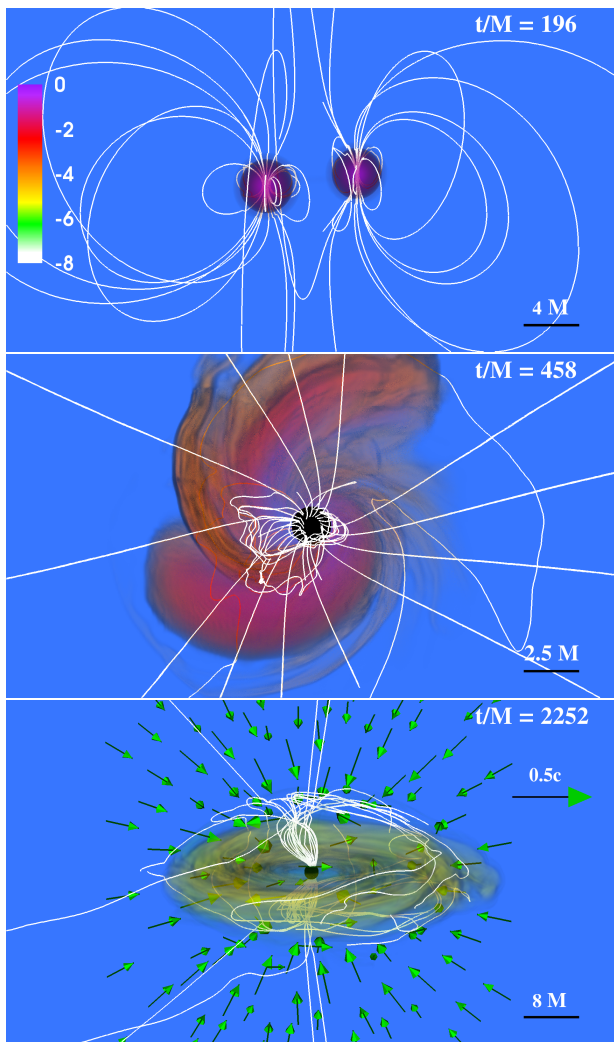


FIG. 1. Volume rendering of rest-mass density  $\rho_0$  normalized to its initial maximum value  $\rho_{0,max} = 7.9 \times 10^{14} (1.8M_\odot/M_{NS})^2 \text{ g/cm}^3$  (log scale) at selected times for the P-Prompt-3 case (see Table I). The top panel shows the time at which the stars are seeded with the B-field (white lines) generated by the vector potential  $A_\phi$  in Eq. (6), the middle panel shows a top view during the BH formation (the black sphere), and the bottom panel shows the end of the simulation. Arrows indicate plasma velocities. Here  $M = 1.1 \times 10^{-2} (M_{NS}/1.8M_\odot) \text{ ms} = 3.31 (M_{NS}/1.8M_\odot) \text{ km}$ .

The spatial discretization is performed by using fourth-order accurate, cell-centered, finite-differencing stencils, except on shift advection terms, where fourth-order accurate upwind stencils are used [56]. Outgoing wave-like boundary conditions are applied to all the evolved variables. The time integration is performed via the method of lines using a fourth-order accurate, Runge-Kutta integration scheme.

**MHD evolution:** The Illinois code solves the equations of ideal GRMHD in a conservative scheme via high-resolution shock capturing methods to handle shocks [66]. For that it

adopts the conservative variables [59]

$$\rho_* \equiv -\sqrt{\gamma} \rho_0 n_\mu u^\mu, \quad (2)$$

$$\tilde{S}_i \equiv -\sqrt{\gamma} T_{\mu\nu} n^\mu \gamma_i^\nu, \quad (3)$$

$$\tilde{\tau} \equiv \sqrt{\gamma} T_{\mu\nu} n^\mu n^\nu - \rho_*, \quad (4)$$

where

$$T_{\mu\nu} = (\rho_0 h + b^2) u_\mu u_\nu + \left( P + \frac{b^2}{2} \right) g_{\mu\nu} - b_\mu b_\nu, \quad (5)$$

is the stress-energy tensor for a magnetized plasma with rest-mass density  $\rho_0$ , pressure  $P$ , specific enthalpy  $h = 1 + \epsilon + P/\rho_0$ , specific internal energy  $\epsilon$ , B-field  $b^\mu = B_{(u)}^\mu / (4\pi)^{1/2}$  as measured by an observer co-moving with the fluid, and  $u^\mu$  the fluid four-velocity. The resulting equations of motion are obtained via the rest-mass and energy-momentum conservation laws (see Eqs. (27)-(29) in [59]). To guarantee that the B-field remains divergenceless during the whole evolution, the code solves the magnetic induction equation using a vector potential  $\mathcal{A}^\mu$  (see Eqs. (8)-(9) in [58]). We also adopt the generalized Lorenz gauge [58, 67] with a damping parameter  $\xi = 16/M$ . This gauge avoids the development of spurious B-fields that arise due to interpolations across the refinement levels in moving-box simulations. As pointed out in [58, 68], interpolations at moving-box boundaries in  $\mathcal{A}^\mu$ -evolution codes may produce spurious conversion of EM gauge modes into physical modes and vice-versa, and as a result spurious B-fields will eventually contaminate the evolution [58]. We close the system of equations in the MHD sector by using a  $\Gamma$ -law equation of state  $P = (\Gamma - 1)\rho_0 \epsilon$ , with  $\Gamma = 2$  to model the NS matter. Finally, as is done in many hydrodynamic and ideal MHD codes, we add a tenuous atmosphere  $\rho_{atm}$  in the grid points where the rest-mass density is below a threshold value. We set  $\rho_{atm} = 10^{-10} \rho_{max}$ , where  $\rho_{max}$  is the maximum value of the initial rest-mass density of the system [59].

## B. Initial data

NSNS mergers may yield a remnant that can either form a transient differentially-rotating HMNS that can survive for many rotation periods [55], or promptly collapse to a BH. The above outcome depends strongly of the *total* mass of the system, and independently of the mass ratio. If the total rest mass of a  $\Gamma = 2$  EOS NSNS binary is  $\gtrsim 3.44M_\odot (k/262.7\text{km}^2)^{1/2}$ , then the system will promptly collapse to a BH. This mass corresponds to  $\sim 1.7$  times the maximum allowed rest mass of a single spherical NS, which turns out to be  $M_{\text{sph}} \approx 1.98M_\odot (k/262.7\text{km}^2)^{1/2}$ , or a total ADM mass of  $M_{\text{sph}}^{\text{ADM}} = 1.8M_\odot (k/262.7\text{km}^2)^{1/2}$ . Note that these results scale with the polytropic constant  $k = P/\rho_0^\Gamma$ , which determines the TolmanOppenheimerVolkoff (TOV) maximum mass. Besides, the threshold mass depends strongly on the EOS. Namely, for realistic EOSs, such as APR or SLy, the threshold mass is  $\sim 1.3 - 1.35 M_{\text{sph}}$  (see e.g. [40–42]).

We consider NSNS binaries in quasiequilibrium circular orbits that inspiral, merge and undergo prompt collapse. The

TABLE I. Initial data for the NSNS prompt collapse cases, as well as the delayed collapse case considered in [27]. All the models have an initial separation of  $44.42 (k/k_0)^{1/2} \text{km}$ , where  $k_0 = 262.7 \text{km}^2$ . Columns show the compaction  $(M/R)_i$  of each companion  $i = 1, 2$ , which is computed assuming an isolated spherical star with the same rest mass, the coordinate equatorial radius of each star  $R_{\text{eq}_i}$ , the total rest mass  $M_0$ , the ADM mass  $M_{\text{ADM}}$ , the ADM angular momentum  $J_{\text{ADM}}$ , and the binary angular frequency  $\Omega$ . These models are also listed in Tables III-IV of [65]. For completeness, we include the initial magnetic energy in units of  $10^{50} \text{erg s}^{-1}$  as defined in Eq. (9) for models P and I, respectively.

Model	$(M/R)_1$	$(M/R)_2$	$R_{\text{eq}_1} (k/k_0)^{1/2}$	$R_{\text{eq}_2} (k/k_0)^{1/2}$	$M_0 (k/k_0)^{1/2}$	$M_{\text{ADM}} (k/k_0)^{1/2}$	$J_{\text{ADM}} (k/k_0)$	$\Omega (k_0/k)^{1/2}$	$\mathcal{M}$
Prompt-1	0.16	0.16	12.2	12.2 km	$3.51 M_\odot$	$3.22 M_\odot$	$9.87 M_\odot^2$	$1914.7 \text{ s}^{-1}$	1.2, 1.4
Prompt-2	0.18	0.18	11.0	11.0 km	$3.75 M_\odot$	$3.40 M_\odot$	$10.90 M_\odot^2$	$2218.6 \text{ s}^{-1}$	2.0, 1.8
Prompt-3	0.16	0.18	12.2	11.1 km	$3.63 M_\odot$	$3.31 M_\odot$	$10.37 M_\odot^2$	$2188.2 \text{ s}^{-1}$	1.7, 1.8
Delayed	0.14	0.14	13.5	13.5 km	$3.20 M_\odot$	$2.96 M_\odot$	$8.61 M_\odot^2$	$1884.3 \text{ s}^{-1}$	1.4, 3.2

initial stars are irrotational,  $\Gamma = 2$  polytropes, and we evolve the matter with a  $\Gamma$ -law EoS, allowing for shock heating. The initial data are computed using the publicly available LORENE code <sup>4</sup>. All our models have an initial separation of  $44.42 (k/262.7 \text{km}^2)^{1/2} \text{km}$ . Table I summarizes the initial parameters of the models considered. For comparison purposes, we also include the NSNS delayed case treated previously in [27].

As in [26, 27], and to avoid build up of numerical errors, we evolve the above initial data until approximately two orbits before merger. At that time,  $t = t_B$ , the NSs are endowed with a dynamically unimportant interior B-field using one of the following two prescriptions:

- **Pulsar case:** In the pulsar case (hereafter the P case), the stars are seeded with a dipolar B-field generated by the vector potential [67, 69]

$$A_\phi = \frac{\pi \varpi^2 I_0 r_0^2}{(r_0^2 + r^2)^{3/2}} \left[ 1 + \frac{15 r_0^2 (r_0^2 + \varpi^2)}{8 (r_0^2 + r^2)^2} \right], \quad (6)$$

that approximately corresponds to that generated by an interior current loop (see top panel of Fig. 1). Here  $r_0$  is the current loop radius,  $I_0$  is the current,  $r^2 = \varpi^2 + z^2$ , with  $\varpi^2 = (x - x_{\text{NS}})^2 + (y - y_{\text{NS}})^2$ , and  $(x_{\text{NS}}, y_{\text{NS}})$  is the position of the NS centroid. We choose the current  $I_0$  and radius of the loop  $r_0$  such that the maximum value of the magnetic-to-gas-pressure ratio in the NS interior is  $\beta^{-1} \equiv P_{\text{mag}}/P_{\text{gas}} = 0.003125$  (see Fig. 2) which matches the value used in [27]. The resulting B-field strength at the NS pole turns out to be  $B_{\text{pole}} \approx 1.58 \times 10^{15} (1.8 M_\odot / M_{\text{NS}}) \text{G}$ . This B-field was chosen in [27] so that the rms value of the B-field in the transient HMNS is similar to that reported in the very high resolution NSNS simulations [32], where it was shown that during the NSNS merger both the KHI and the MRI can boost the B-field strength to values from  $\sim 10^{13} \text{G}$  to  $\sim 10^{15.5} \text{G}$ , with local values up to  $\sim 10^{17} \text{G}$ . Finally, to reliably evolve the B-field in the stellar exterior and, at the same time, mimic the low

$\beta_{\text{ext}}$  environment that characterizes a force-free, pulsar-like magnetosphere, a new tenuous and variable density atmosphere satisfying  $\beta_{\text{ext}}^{-1} = 100$  everywhere in the exterior is initially imposed at  $t = t_B$  on top of  $\rho_{\text{atm}}$ , as we did in [26, 27] (see Fig. 2). Since the dipole B-field strength falls away from the NS surface as  $1/r^3$ , this prescription forces the variable density in the atmosphere also to fall initially as  $1/r^3$  until it equals  $\rho_{\text{atm}}$ . Subsequently, all the dynamical variables, interior and exterior, are evolved according to the ideal GRMHD equations. This artificial atmosphere increases the total rest-mass of the system by less than  $\sim 1.0\%$ .

TABLE II. List of grid parameters for all models listed in Table I. The computational mesh consists of two sets of seven nested grids centered one on each of the NSs. Here  $\Delta x_{\text{max}}$  is the coarsest grid spacing. The grid spacing of all other levels is  $\Delta x_{\text{max}}/2^{n-1}$  with  $n = 2, \dots, 7$ . Here  $M$  is the total rest-mass of the system.

Model	$\Delta x_{\text{max}}$	Grid hierarchy
Prompt-1	$1.84M$	$213.22M/2^{n-1}$
Prompt-2	$1.56M$	$182.35M/2^{n-1}$
Prompt-3	$1.78M$	$207.04M/2^{n-1}$
Delayed	$2.20M$	$245.66M/2^{n-1}$

- **Interior case:** In the interior case (hereafter the I case) the stars are seeded with a poloidal B-field confined to the NS interior through the vector potential [57]

$$A_i = C_i \varpi^2 \max(P - P_{\text{cut}}, 0)^{n_b}, \quad (7)$$

with

$$C_i = \left( -\frac{y - y_{\text{NS}}}{\varpi^2} \delta^x_i + \frac{x - x_{\text{NS}}}{\varpi^2} \delta^y_i \right) A_b, \quad (8)$$

where  $A_b$ ,  $n_b$  and  $P_{\text{cut}}$  are free parameters that parametrize the strength, the degree of central condensation and the confinement of the B-field, respectively. We set  $P_{\text{cut}} = 0.01 \max(P)$  and  $n_b = 1$ , and then  $A_b$  is chosen so that the resulting B-field at the center of each star coincides with that in the P-cases.

<sup>4</sup> <http://www.lorene.obspm.fr>

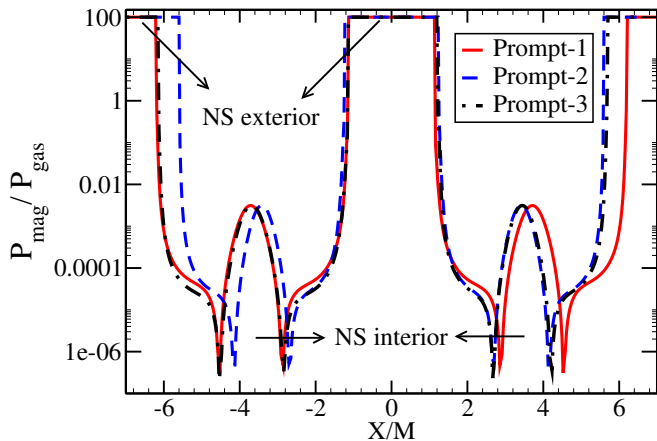


FIG. 2. Magnetic-to-gas pressure ratio  $\beta^{-1} \equiv P_{\text{mag}}/P_{\text{gas}}$  at the time a dipole-like B-field is seeded in the NSNS cases listed in Table I. The B-field is generated by the vector potential  $A_\phi$  given by Eq. (6). Here the two NS are centered at  $x/M = \pm 3.45$  in the Prompt-1 case, and at  $x/M = \pm 3.67$  in the Prompt-2 case, and  $y/M = z/M = 0$ . Notice that the position of each of the NSs in the Prompt-3 case matches the position of the corresponding companion with the same mass and compaction as in the above cases (see Table I).

In all our cases (see Table I), the magnetic-to-orbital-binding-energy ratio as defined in [70] is  $\sim 1.45 \times 10^{-6}$  and the magnetic dipole moment is aligned with the orbital angular momentum of the system.

### C. Grid structure

The numerical grids consist of two sets of refinement boxes centered on each of the NSs. Once they overlap they are replaced by a common box centered on the system center of mass. Each set consists of seven boxes that differ in size and in resolution by factors of two. The finest box around each NS has a side half-length of  $\sim 1.3 R_{\text{NS}}$ , where  $R_{\text{NS}}$  is the initial NS equatorial radius (see Table I). The grid structure of the mesh refinement used in the simulations is listed in Table II. In all cases, the initial NS diameter is resolved by  $\sim 180$  grid points. We impose reflection symmetry across the orbital plane. Note that this resolution matches the high resolution used in [27].

### D. Diagnostic quantities

During the whole evolution we monitor several diagnostic quantities to verify the reliability of our numerical calculations. We monitor the normalized Hamiltonian and momentum constraints defined by Eqs. (40)-(43) in [56]. In all cases listed in Table I, the constraint violations are below 0.03 throughout the evolution. As expected the constraints peak during BH formation and then decrease as the evolution proceeds. We use the `AHFinderDirect` thorn [71] to locate and monitor the apparent horizon. To estimate the BH mass

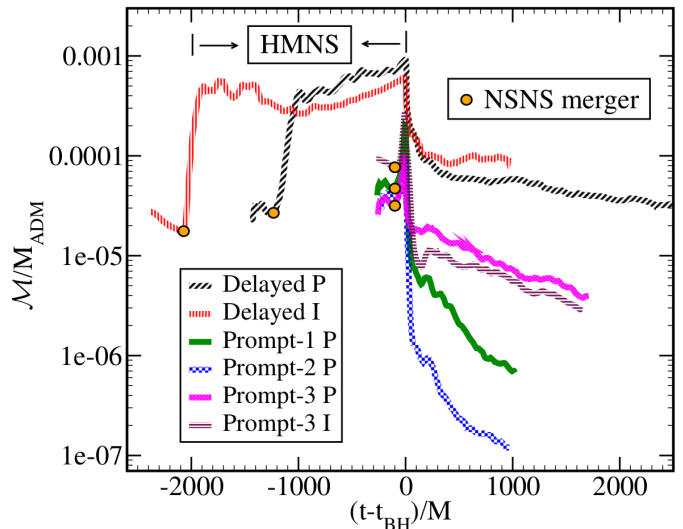


FIG. 3. Total magnetic energy  $\mathcal{M}$  (normalized by the ADM mass) vs. time for cases in Table I. Dots indicate the NSNS merger time. The horizontal axis has been shifted to the BH formation time. In contrast to the delayed collapse, magnetic instabilities during the HMNS epoch steeply amplify the magnetic energy  $\mathcal{M}$ .

$M_{\text{BH}}$  and its dimensionless spin parameter  $a_{\text{BH}}/M_{\text{BH}}$  we use Eqs. (5.2)-(5.3) in [72].

To measure the energy and angular momentum radiated in form of GWs, we use a modified version of the `Psikadelia` thorn that computes the Weyl scalar  $\Psi_4$ , which is decomposed into  $s = -2$  spin-weighted spherical harmonics (see e.g. [73]) at different radii between  $\approx 30M \sim 135(M_{\text{NS}}/1.8M_\odot)\text{km}$  and  $\approx 160M \sim 710(M_{\text{NS}}/1.8M_\odot)\text{km}$ . We find that between  $\sim 0.2\%$  and  $\sim 0.4\%$  of the energy of our models is radiated away in form of gravitational radiation, while between  $\sim 1.8\%$  and  $\sim 3.4\%$  of the angular momentum is radiated. We also compute the outgoing EM (Poynting) luminosity  $L_{\text{EM}} \equiv -\int T_t^{r(\text{EM})} \sqrt{-g} dS$  across a given surface  $S$ , where  $T_{\mu\nu}^{(\text{EM})}$  is the electromagnetic energy-momentum tensor. Using Eqs. (21)-(22) in [57], and taking into account the GW and EM radiation losses, we verify the conservation of the total mass  $M_{\text{int}}$  and the total angular momentum  $J_{\text{int}}$ , which coincide with the ADM mass and ADM angular momentum of the system at spatial infinity. In all cases the total mass is conserved to within  $\sim 1\%$ , and the total angular momentum is conserved to within  $\sim 8\%$ . Finally, we monitor the magnetic energy

$$\mathcal{M} = \int u^\mu u^\nu T_{\mu\nu}^{(\text{EM})} dV, \quad (9)$$

measured by a comoving observer [57]. Here  $dV = e^{6\phi} d^3x$  is the proper volume element on a spatial slice. Once the BH forms,  $\mathcal{M}$  is calculated in the fluid exterior of the horizon.



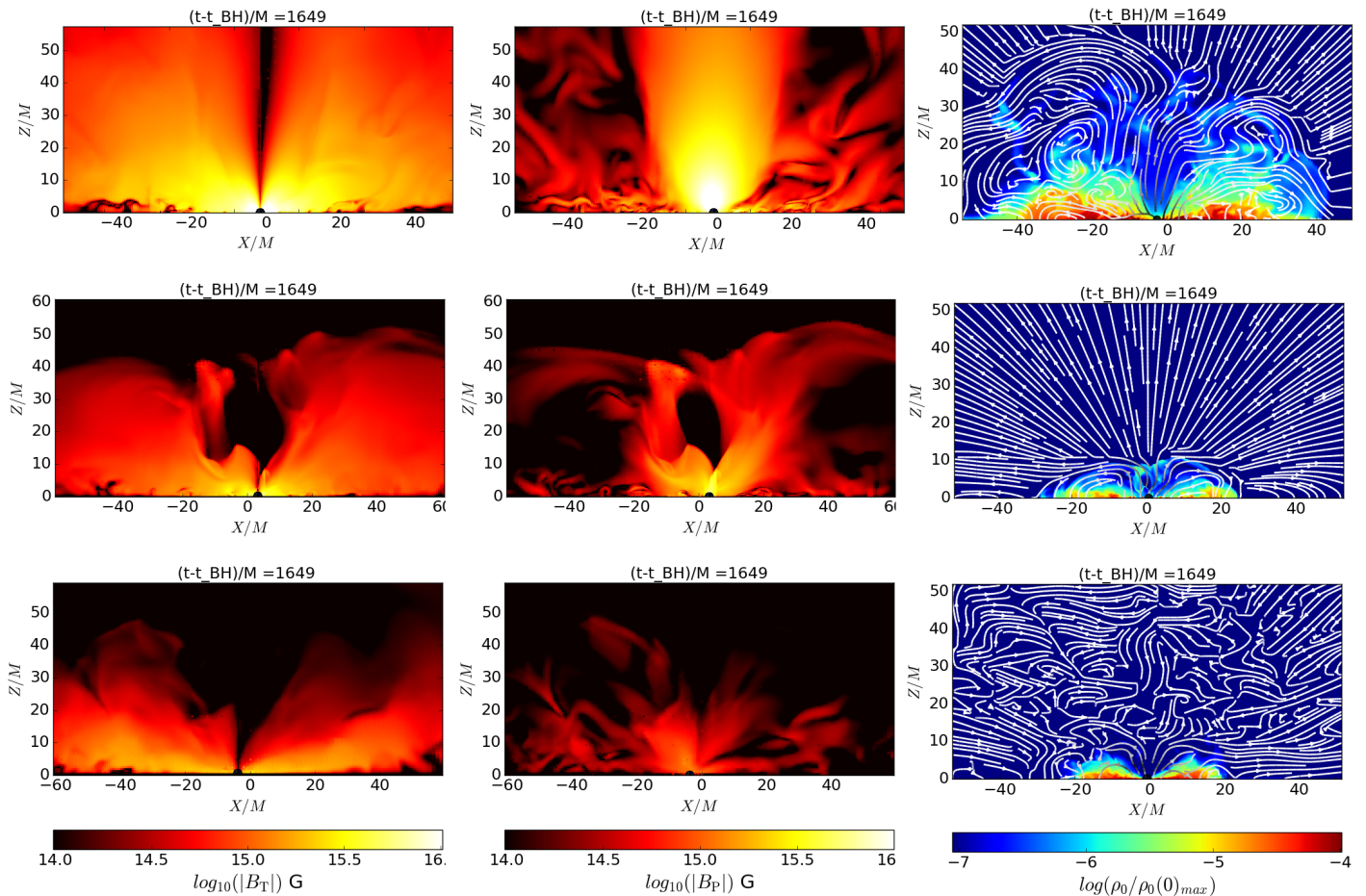


FIG. 4. Toroidal (left column) and poloidal (middle column) components of the B-field, and rest-mass density normalized to its maximum value (right column) on a meridional plane near the end of the prompt-3 cases. Top panel shows the P-Delayed case, while the P-Prompt-3 and the I-Prompt-3 cases are shown in the middle and the bottom panels, respectively. The white lines on the right panel show the B-field structure, while the central black disks in all panels denote the apparent horizons. Notice that only in the delayed collapse case, the two components of the B-field have a strength  $\gtrsim 10^{15.7} (1.8M_{\odot}/M_{NS})G$ .

### III. RESULTS

The evolution of our binary NS models can be characterized by three phases: inspiral, plunge-and-merger, and a spinning BH remnant surrounded by a disk of magnetized tidal debris that accretes onto it. During the inspiral, the orbital separation between the stars decreases adiabatically as the energy and angular momentum are radiated by GWs (the radiated EM energy during this phase is much smaller than the GW emission). Once the quasi-circular inspiral orbit becomes unstable, the stars plunge and merge. Depending on the total mass of the system, the merged stars will promptly collapse or will form a HMNS. During the last two phases of the evolution, magnetically driven outflows and/or strong EM signals can be produced that may explain or give new insight regarding sGRB phenomenology.

In the following section, we briefly summarize the dynamics of the delayed collapse cases previously performed in [27]. We then describe the dynamics of the prompt collapse cases

displayed in Table I and highlight the principle differences with respect to the delayed case. Since the dynamics, GWs, and EM signals are qualitative the same in the six prompt collapse cases, we mainly discuss the merger and the final outcome of the P-Prompt-3 case. Key results from our models are displayed in Table III.

#### A. Delayed collapse

As the magnetic-to-gas-pressure ratio in the NS interior is initially small ( $\beta^{-1} \ll 1$ ), the late inspiral phase of the NSNS systems proceed basically unperturbed by the B-field. The frozen-in B-field is simply dragged by the fluid stars and the magnetic energy  $\mathcal{M}$  does not change significantly (see Fig. 3). Note that recently an enhancement of the magnetic energy during the early inspiral was reported in [31, 36]. This behavior may be related to tidal deformation during this epoch.

GW emission drives the system to the plunge-and-merger phase, and after  $t - t_B \sim 230M \approx 3.60(M_{NS}/1.8M_{\odot})ms$

following the B-field insertion, the NSs come into contact and form a differentially rotating HMNS. During merger leading delayed collapse, the magnetic energy is steeply amplified. We find that by  $t - t_{\text{merger}} \sim 256M \approx 3.8(M_{\text{NS}}/1.8M_{\odot})\text{ms}$  following the merger,  $\mathcal{M}$  is amplified  $\sim 12$  times its initial value (see Fig. 3). Note that a similar behavior was reported in very high resolution simulations [31], which was attributed to both the KHI and MRI.

Once the system settles down to a quasiequilibrium HMNS, a strong toroidal B-field is generated, mainly due winding by differential rotation. As a result  $\mathcal{M}$  is further amplified (by a factor of  $\sim 1.7$  in the P-Delayed case, and  $\sim 1.3$  in the I-Delayed case). This behavior was expected since the initial B-field was chosen such that the magnetic energy may reach equipartition with the kinetic energy during merger and HMNS evolution, as was suggested previously in [31]. We find that the wavelength  $\lambda_{\text{MRI}}$  of the fastest growing MRI is resolved by  $\gtrsim 10$  grid points and it fits within the star [74]. We also find that the MRI timescale is  $\tau_{\text{MRI}} \sim \Omega^{-1} \sim 40 - 100(M_{\text{NS}}/1.8M_{\odot})^{1/2}\text{km} \sim 0.13 - 0.33(M_{\text{NS}}/1.8M_{\odot})^{1/2}\text{ms}$  (for details see [75]). Here  $\Omega$  is the angular velocity of the HMNS. Thus, it is likely that the MRI is properly captured and operating in the system. Magnetic winding drives the HMNS toward uniform rotation [76] and, since the rest mass of the star remnant exceeds the maximum value allowed by uniform rotation (i.e. the ‘‘supramassive’’ limit,  $M_0 \approx 2.36M_{\odot}(k/262.7\text{km}^2)$  for  $\Gamma = 2$  EOS [77]), it eventually collapses to a BH, with mass  $M_{\text{BH}} \approx 2.81M_{\odot}(M_{\text{NS}}/1.8M_{\odot})$  and spin parameter  $a/M_{\text{BH}} \simeq 0.74$ , surrounded by a highly magnetized accretion disk (see top panels of Fig. 4). Just after collapse, we find that the rms value of the B-field in the disk is  $\sim 10^{15.9}(1.8M_{\odot}/M_{\text{NS}})\text{G}$ .

During the collapse, the inner layers of the HMNS, which contain most of the magnetic energy, are quickly swallowed by the BH, and thus the magnetic energy  $\mathcal{M}$  steeply decreases during  $t - t_{\text{BH}} \sim 63M \approx 1(M_{\text{NS}}/1.8M_{\odot})\text{ms}$ , until the accretion disk settles down, after which  $\mathcal{M}$  slightly decreases as the magnetized material is accreted (see Fig 3). Near to the end of the simulation, the magnetic energy is  $\mathcal{M} \sim 7.2 \times 10^{49}(M_{\text{NS}}/1.8M_{\odot})\text{ergs}$ . Similar values were reported in very high resolution simulations [31].

As the accretion proceeds, the force-free parameter  $B^2/(8\pi\rho_0) = b^2/(2\rho_0)$  gradually grows as the regions above the BH poles are getting cleaned out of fall-back material (see right panel of Fig. 5). Once the exterior is magnetically-dominated, the magnetic pressure above the BH poles is high enough to overcome the ram pressure produced by the fall-back material. We observe that when the force-free parameter reaches values  $\gtrsim 10$ , fluid velocities begin to turn. By  $t - t_{\text{BH}} \sim 2900M \approx 45.42(M_{\text{NS}}/1.8M_{\odot})\text{ms}$ , a magnetically driven outflow extends to heights  $\geq 100M \approx 470(M_{\text{NS}}/1.8M_{\odot})\text{km}$ , and an incipient jet has been launched. Near the end of the simulation, the Lorentz factor inside the funnel is  $\Gamma_L \sim 1.2$  and thus the jet is only mildly relativistic. However, we also find that, at that time, the space-average value of  $b^2/(2\rho_0)$  in a cubical region with length side of  $2r_{\text{BH}}$  above the BH has grown to  $\sim 10^{2.2}$  (see Fig. 6) and is thus becoming force-free. Since

the terminal Lorentz factor of a magnetically driven, axisymmetric jet is comparable to this parameter [78], the jet may be accelerated to higher Lorentz factors. Here  $r_{\text{BH}}$  is the radius of the BH horizon. Near the end of the simulation, the rms value of the the B-field is  $\sim 10^{15.9}(1.8M_{\odot}/M_{\text{NS}})\text{G}$ . See Table III for the I-Delayed case. Based on the accretion rate and the mass of the accretion disk, we find that the disk will be accreted in  $\Delta t \sim M_{\text{disk}}/\dot{M} \sim 97\text{ms}$ , which is consistent with timescales of short duration sGRBs [33]. The angular frequency of the B-field and the outgoing EM luminosity are consistent with those expected from the Blandford–Znajek mechanism [79], as we discussed in [26, 27].

## B. Prompt collapse

As in the above scenario, during the NSNS inspiral the magnetic energy  $\mathcal{M}$  hardly changes, as the dynamically unimportant, frozen-in B-field is advected with the fluid (see Fig. 3). GW emission drives the system to the plunge-and-merger phase, and after  $t - t_B \sim 170M \approx 2.78(M_{\text{NS}}/1.8M_{\odot})\text{ms}$  following the B-field insertion the stars merge, forming a double core structure. The core collapses promptly to a highly spinning BH after  $t - t_{\text{merger}} \sim 80M \approx 1.3(M_{\text{NS}}/1.8M_{\odot})\text{ms}$  following the merger of the two cores (see middle panel in Fig. 1). The BH settles to a mass of  $M_{\text{BH}} \approx 3.1M_{\odot}(M_{\text{NS}}/1.8M_{\odot})$  and spin parameter  $a/M \simeq 0.82$ , consistent with [41, 48]. See Table III for the other cases.

During the NSNS merger, but before the merger of the two dense cores, the magnetic energy  $\mathcal{M}$  is quickly amplified until BH formation (see Fig. 3). In contrast to the delayed collapse case, where the HMNS stage allows the magnetic energy to grow a factor of  $\sim 12$  (see above), we find that  $\mathcal{M}$  is amplified only  $\lesssim 4$  times its initial value.

As the low-density layers of the merging NSs wrap around the BH to form the accretion disk, the B-field is stretched and wound, producing a strong toroidal B-field component (see middle and bottom panels in Fig 4). Just after collapse, the rms value of the toroidal component of the B-field is  $\sim 10^{15.1}(1.8M_{\odot}/M_{\text{NS}})\text{G}$  for the P-Prompt-3 case, and  $\sim 10^{14.7}(1.8M_{\odot}/M_{\text{NS}})\text{G}$  for the I-Prompt-3 case. These values change only slightly during the subsequent evolution (see below). We find that the wavelength of  $\lambda_{\text{MRI}}$  is resolved by more than  $\gtrsim 10$  grid points but only partially fits in the accretion disk [74]. As shown in the right panels of Fig. 4, the accretion disk is not only lighter than the disk in delayed collapse (see Table III), but also two times smaller. It is more difficult to properly resolve the MRI in the prompt collapse case. Here  $\Omega$  is the angular velocity of the accretion disk. However, we do observe indications of turbulence in the disk on meridional slices which may be produced by the existence of unstable global modes [81]. We also find that the effective Shakura–Sunyaev  $\alpha$ -parameter, as defended in [74], which associated with the magnetic stresses is  $\alpha = 0.07 - 0.4$ , consistent with GRMHD simulations of accretion

TABLE III. Summary of main results. Here  $M_{\text{BH}}$  is the mass of the BH remnant in units of  $M_{\odot}$  ( $M_{\text{NS}}/1.8M_{\odot}$ ),  $a/M_{\text{BH}}$  its spin parameter,  $b^2/(2\rho_0)_{\text{ave}}$  is the space-averaged value of the magnetic-to-rest-mass-density ratio over all the grid points inside a cubical region of length  $2r_{\text{BH}}$  above the BH pole (see bottom panel of Fig. 5 and Fig. 6),  $r_{\text{BH}}$  is the radius of the BH apparent horizon,  $B_{\text{rms}}$  denotes the rms value of the B-field above the BH poles in units of  $(1.8M_{\odot}/M_{\text{NS}})\text{G}$ ,  $M_{\text{disk}}/M_0$  is the ratio of the disk rest-mass to the initial total rest mass,  $\dot{M}$  is the accretion rate computed via Eq. (A11) in [80],  $\tau_{\text{disk}} \sim M_{\text{disk}}/\dot{M}$  is the disk lifetime in units of  $(M_{\text{NS}}/1.8M_{\odot})\text{ms}$ ,  $L_{\text{EM}}$  is the Poynting luminosity driven by the incipient jet for the delayed collapse time-averaged over the last 500M  $\sim 7.3(M_{\text{NS}}/1.8M_{\odot})\text{ms}$  of the evolution.

Case Model	$M_{\text{BH}}$	$a/M_{\text{BH}}$	$b^2/(2\rho_0)_{\text{ave}}$	$B_{\text{rms}}$	$M_{\text{disk}}/M_0$	$\dot{M}(M_{\odot}/s)$	$\tau_{\text{disk}}$	$L_{\text{EM}} \text{ erg s}^{-1}$
P-Prompt-1	3.02	0.83	$10^{-2}$	$10^{14.6}$	0.13%	0.34	13.4	—
I-Prompt-1	3.00	0.83	$10^{-6}$	$10^{13.3}$	0.036%	0.08	15.8	—
P-Prompt-2	3.23	0.80	$10^{-3}$	$10^{14.5}$	0.085%	0.23	13.8	—
I-Prompt-2	3.22	0.80	$10^{-6}$	$10^{13.3}$	0.011%	0.02	20.6	—
P-Prompt-3	3.11	0.81	$10^{-1}$	$10^{15.1}$	0.20%	0.36	20.1	—
I-Prompt-3	3.11	0.81	$10^{-1}$	$10^{14.7}$	0.20%	0.37	19.6	—
P-Delayed	2.81	0.74	$10^{2.2}$	$10^{15.9}$	1.0%	0.33	97.0	$10^{51.3}$
I-Delayed	2.81	0.74	$10^{1.5}$	$10^{15.7}$	1.5%	0.77	62.3	$10^{50.7}$

disks around highly spinning BHs [82]. Finally, we find that the MRI timescale is  $\tau_{\text{MRI}} \sim 25 - 100 (M_{\text{NS}}/1.8M_{\odot})^{1/2}\text{km} \sim 0.08 - 0.33(M_{\text{NS}}/1.8M_{\odot})^{1/2}\text{ms}$ . Thus, it is likely that magnetically-driven turbulence is operating, at least partially, in our system.

We follow the evolution of the BH-disk remnant for around  $t - t_{\text{merger}} \sim 1650M \approx 26.74(M_{\text{NS}}/1.8M_{\odot})\text{ms}$  after merger, which corresponds to  $\sim 5.3$  Alfvén time scales. No further enhancement in the magnetic energy was observed. In fact, as it is shown in Fig. 3, as the accretion proceeds,  $\mathcal{M}$  gradually decreases. Near the end of the simulation, the magnetic energy is  $\mathcal{M} \approx 2.65 \times 10^{48} (M_{\text{NS}}/1.8M_{\odot}) \text{ergs}$ , a factor of  $\sim 30$  smaller than in the delayed case.

As the matter above the BH poles is accreted, meridional slices (see Fig. 5) show the expansion of regions where the force-free parameter reaches values of  $b^2/(2\rho_0) \approx 10^{-0.6}$  (quasi-magnetic dominated regions). We observe that after  $t - t_{\text{BH}} \sim 1000M \approx 16.2(M_{\text{NS}}/1.8M_{\odot})\text{ms}$ , the magnetic pressure is high enough to push material upward until it balances the ram pressure at a height of  $\sim 8r_{\text{BH}}$  (see middle and right panels of Fig. 5). After that point, the system settles down. The quasi-magnetically dominated regions bounce up and down above the BH poles, but they never escape. Fig. 5 shows a side by side comparison of these regions in the P-Delayed case (left panel) and P-Prompt-3 and I-Prompt-3 cases (middle and right panels, respectively) on a meridional slice at three different times: at BH formation, at about halfway and near the end of the simulations of the Prompt-3 cases. As it can be seen, at the BH formation time, there are no magnetically dominated force-free regions in any of the two Prompt collapse cases. In contrast, in the delayed case, these regions extend to  $\sim 10r_{\text{BH}}$  above the BH poles. As the evolution proceeds,  $b^2/(2\rho_0)$  gets larger in all the three cases. However, while in the delayed collapse case these regions continuously expand as the accretion proceeds, in the prompt collapse cases the force-free parameter settles down. To verify this, we compute the space-averaged value of  $b^2/(2\rho_0)$  on a cubical region of a length side  $2r_{\text{BH}}$  just above the BH poles during the evo-

lution (see bottom panels of Fig.5). We find that the average value the force-free parameter in both the P-Prompt-3 and the I-prompt-3 cases reaches a value of  $b^2/(2\rho_0)_{\text{ave}} \sim 10^{-1}$  after  $\sim 800M \approx 13(M_{\text{NS}}/1.8M_{\odot})\text{ms}$  and then settles down (see Fig. 6). In the delayed collapse case, in contrast, the averaged value monotonically increases with time, whereby by  $t - t_{\text{BH}} \sim 2900M \sim 42.2(M_{\text{NS}}/1.8M_{\odot})$ , near the end of the simulation, the force-free parameter reaches a value of  $b^2/(2\rho_0)_{\text{ave}} \sim 10^{2.2}$ . See Table III for the other cases.

We also compare in Fig. 4 the strength of the poloidal and toroidal B-field components as well as the B-field configurations toward the end of the P-Prompt-3 cases. In the three cases, the toroidal component is, as expected, the dominant component in the accretion disk, while in regions above the BH poles the poloidal component dominates. Notice that only in the delayed collapse case does the B-field reach equipartition-strength values ( $\gtrsim 10^{15.7} (1.8M_{\odot}/M_{\text{NS}})\text{G}$ ) in both the disk and in the funnel, which reinforces the fact that if the B-field in NSNS mergers can be amplified to equipartition levels then, the system provides a viable model for sGRBs [27, 31]. See Table III for the other cases. Finally, notice that, as shown in the right panel of Fig. 4, by  $t - t_{\text{BH}} \sim 1650M \approx 26(M_{\text{NS}}/1.8M_{\odot})\text{ms}$  the winding of the B-field above the BH poles is well underway only in the P-Delayed case. There is no evidence of that effect in any of the prompt collapse cases. So, our results indicate that NSNS mergers can be the progenitors that power sGRBs only if the magnetic energy can be efficiently amplified to equipartition levels [27, 31], which seems to be possible only if a transient HMNS forms, i.e. only in NSNS systems that lead to delayed collapse to BH.

#### IV. CONCLUSIONS

Mergers of NSNSs have been suggested as one of the possible progenitors of sGRBs [10, 11, 83]. This hypothesis has been reinforced by the first detection of a kilonova associate with the system “GRB 130603B” [20, 21]. Using numeri-



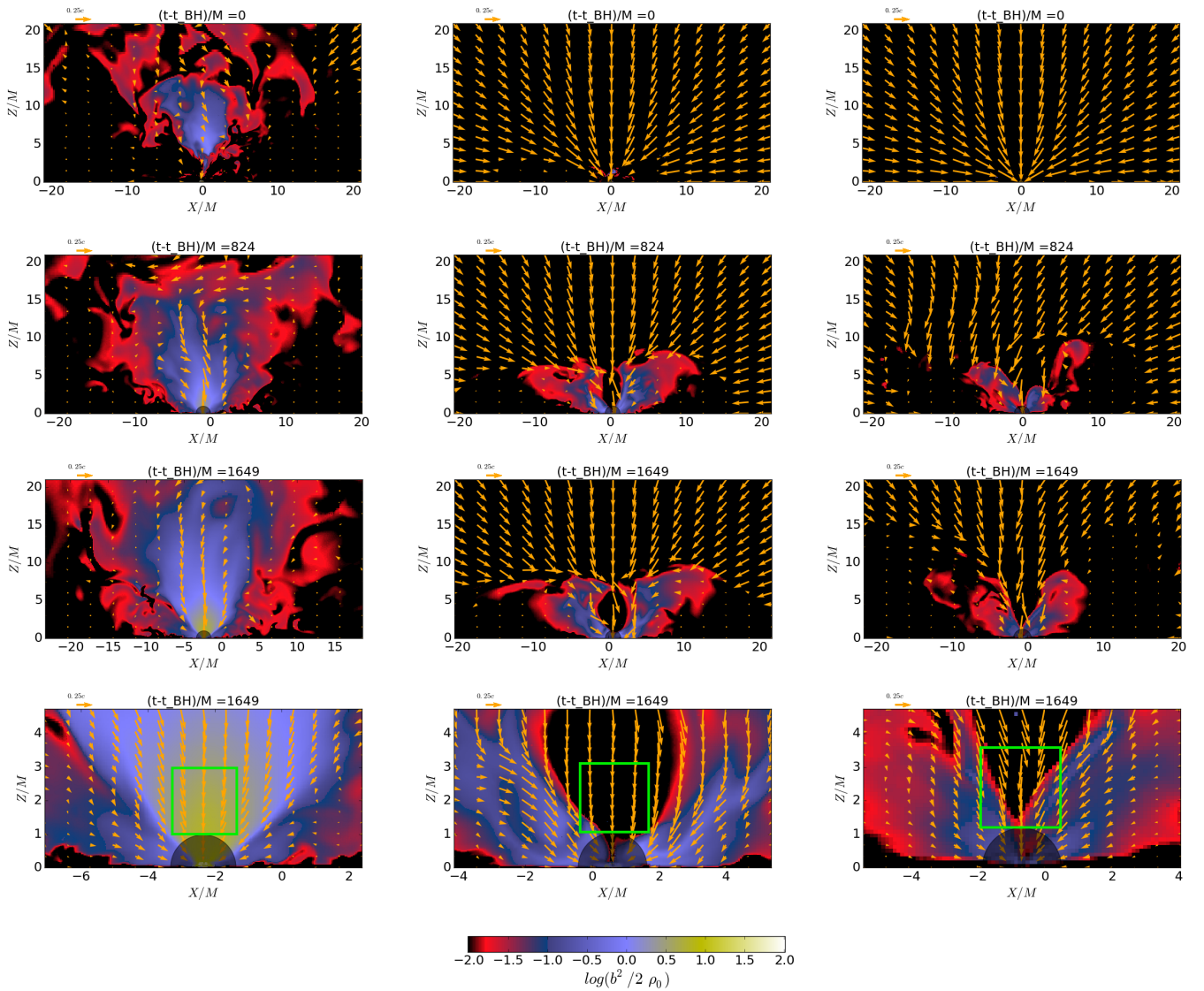


FIG. 5. Force-free parameter  $b^2/(2\rho_0)$  on a meridional plane at selected times for the P-Delayed case (left panel) and the P-Prompt-3 and I-Prompt cases (middle and right panels, respectively). The arrows indicate the plasma velocities, while the black semicircles denotes the BH apparent horizons. Magnetically-dominated force-free areas correspond to regions where  $b^2/(2\rho_0) \geq 1$ . The bottom row is a zoomed-in view of the force-free parameter in Fig 6. The square above the BH pole denotes the cubical region used to compute the average values of the force-free parameter in Fig 6.

cal simulations, we have recently shown [27] that NSNS systems that undergo *delayed* collapse can launch a magnetically-sustained mildly relativistic outflow— an incipient jet. The accretion time scale of the disk and outgoing electromagnetic signals are consistent with sGRBs as well as with the Blandford–Znajek mechanism for launching these jets and associated Poynting luminosities [79].

In this paper, we have performed magnetohydrodynamic simulations in full general relativity of different NSNS configurations that undergo *prompt* collapse (see Table I). The stars possess a B-field that extends from the NS interior into the exterior in some cases, or a B-field that is confined to the NS interior. Our results show that the absence of a HMNS epoch for prompt collapse prevents the magnetic energy from

approaching force-free values above the BH poles. This limitation inhibits the launching of a jet. After  $t - t_{BH} \sim 1000M \sim 16.2(M_{NS}/1.8M_{\odot})\text{ms}$  following the collapse, we did not find any evidence of an outflow or B-field collimation as we did in delayed collapse. At the end of the simulations the rms value of the B-field is  $\lesssim 10^{15.1} (1.8M_{\odot}/M_{NS})\text{G}$  and  $b^2/(2\rho_0) \lesssim 0.1$ . Our results seem to reinforce the previous NSNS studies that claim that only NSNS systems in which the magnetic energy reaches equipartition levels can launch magnetically-supported jets, and may be then progenitors of sGRBs [31]. Notice that, although higher resolution is required to properly capture the KHI and the MRI, we do not expect a significant change in the outcome. The magnetic energy amplification due to these magnetic instabilities oc-

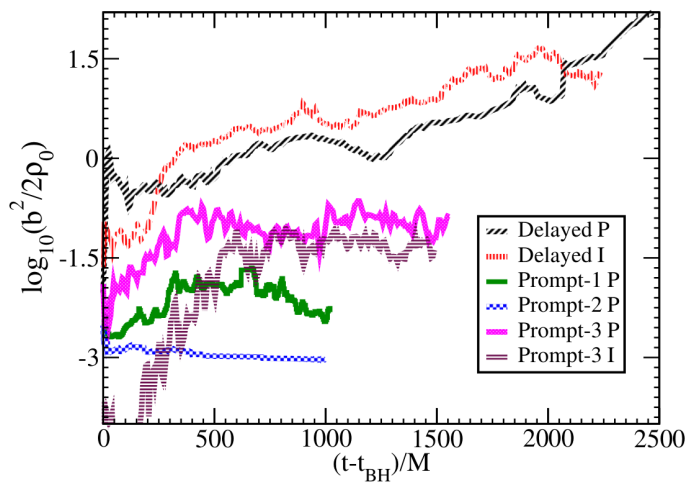


FIG. 6. Average value of the force-free parameter  $b^2/(2\rho_0)$  vs time (log scale). This average is computed using all the grid points contained in a cube of edge  $2r_{BH}$  above the BH as shown in the bottom panel of Fig. 5. Here  $r_{BH}$  denotes the radius of the BH.

curs on an Alfvén timescale ( $\sim 5(M_{NS}/1.8M_{\odot})\text{ms}$ ), but, in the prompt collapse cases, the NSNS remnant collapses on a shorter timescale ( $\sim 1.3(M_{NS}/1.8M_{\odot})\text{ms}$ ) preventing their growth. So, the magnetic energy in these cases cannot reach equipartition levels required to trigger jets.

Although our study is illustrative and not exhaustive, it suggests that coincident detections of gravitational waves with sGRBs may be possible only in delayed collapse but not in the case of prompt collapse. This finding can be used to constrain the EOS if the masses of these stars in the binary can be reliably determined from measurements of the gravitational signals during the pre-merger inspiral phase of a merg-

ing NSNS [51, 52]. For example, if the well-known binary pulsar PSR 1913+16 merges and a GW signal is detected in coincidence with an sGRB then we will know that the EOS that models these stars must have a threshold value for prompt collapse larger than the total mass of this binary ( $\gtrsim 2.83M_{\odot}$ ). Thus, this coincident detection will automatically rule out the SLy and FPS EOSs, whose threshold masses are  $\sim 2.7M_{\odot}$  and  $\sim 2.5M_{\odot}$ , respectively [84, 85]. Additionally, measurement of the time delay between the gravitational peak and sGRBs may provide an estimate of the initial neutron star B-field strength [55].

## ACKNOWLEDGMENTS

We thank Charles Gammie, Roman Gold and Vasileios Paschalidis for useful discussions, and the Illinois Relativity group REU team (Eric Connelly, Cunwei Fan, Patchara Wong-sutthikoson and John Simone) for assistance in creating Fig. 1. This work has been supported in part by National Science Foundation (NSF) Grants PHY-1602536 and PHY-1662211, and NASA Grants NNX13AH44G and 80NSSC17K0070 at the University of Illinois at Urbana-Champaign. This work made use of the Extreme Science and Engineering Discovery Environment (XSEDE), which is supported by National Science Foundation grant number TG-MCA99S008. This research is part of the Blue Waters sustained-petascale computing project, which is supported by the National Science Foundation (awards OCI-0725070 and ACI-1238993) and the State of Illinois. Blue Waters is a joint effort of the University of Illinois at Urbana-Champaign and its National Center for Supercomputing Applications.

- 
- [1] B. P. Abbott *et al.* (Virgo, LIGO Scientific), *Astrophys. J.* **833**, L1 (2016).
  - [2] B. P. Abbott and *et al.* (LIGO Scientific Collaboration and Virgo Collaboration), *Phys. Rev. Lett.* **116**, 061102 (2016).
  - [3] B. Abbott *et al.* (Virgo, LIGO Scientific), *Phys. Rev. Lett.* **116**, 241103 (2016).
  - [4] B. P. Abbott *et al.* (LIGO Scientific and Virgo Collaboration), *Phys. Rev. Lett.* **118**, 221101 (2017).
  - [5] B. P. Abbott *et al.* (VIRGO, LIGO Scientific), (2013), 10.1007/lrr-2016-1, *living Rev. Rel.* 19,1(2016).
  - [6] B. P. Abbott *et al.* (Virgo, LIGO Scientific), *Astrophys. J.* **832**, L21 (2016).
  - [7] M. Dominik, E. Berti, R. O’Shaughnessy, I. Mandel, K. Belczynski, C. Fryer, D. E. Holz, T. Bulik, and F. Pannarale, *Astrophys. J.* **806**, 263 (2015).
  - [8] J. Abadie, B. P. Abbott, R. Abbott, M. Abernathy, T. Accadia, F. Acernese, C. Adams, R. Adhikari, P. Ajith, B. Allen, and *et al.*, *Classical and Quantum Gravity* **27**, 173001 (2010).
  - [9] S. I. Blinnikov, I. D. Novikov, T. V. Perevodchikova, and A. G. Polnarev, *Soviet Astronomy Letters* **10**, 177 (1984).
  - [10] D. Eichler, M. Livio, T. Piran, and D. N. Schramm, *Nature (London)* **340**, 126 (1989).
  - [11] R. Narayan, B. Paczynski, and T. Piran, *apjl* **395**, L83 (1992).
  - [12] B. Paczynski, *apjl* **308**, L43 (1986).
  - [13] T. Piran, in *General Relativity and Gravitation*, edited by N. T. Bishop and D. M. Sunil (2002) p. 259.
  - [14] E. Berger *et al.*, *Nature (London)* **118**, 988 (2005).
  - [15] D. Fox *et al.*, *Nature (London)* **437**, 845 (2005).
  - [16] J. Hjorth *et al.*, *Nature (London)* **437**, 859 (2005).
  - [17] J. S. Bloom *et al.*, *Astrophys. J.* **638**, 354 (2006).
  - [18] L. Baiotti and L. Rezzolla, (2016), arXiv:1607.03540 [gr-qc].
  - [19] V. Paschalidis, *Class. Quant. Grav.* **34**, 084002 (2017).
  - [20] N. R. Tanvir *et al.*, *Nature* **500**, 547 (2013).
  - [21] E. Berger, W. Fong, and R. Chornock, *Astrophys. J.* **774**, L23 (2013).
  - [22] B. D. Lackey and L. Wade, *Phys. Rev.* **D91**, 043002 (2015).
  - [23] Y. Sekiguchi, K. Kiuchi, K. Kyutoku, and M. Shibata, *Phys. Rev.* **D91**, 064059 (2015).
  - [24] Y. Sekiguchi, K. Kiuchi, K. Kyutoku, M. Shibata, and K. Taniguchi, *Phys. Rev.* **D93**, 124046 (2016).
  - [25] F. Foucart, D. Desai, W. Brege, M. D. Duez, D. Kasen, D. A. Hemberger, L. E. Kidder, H. P. Pfeiffer, and M. A. Scheel, *Class. Quant. Grav.* **34**, 044002 (2017).

- [26] V. Paschalidis, M. Ruiz, and S. L. Shapiro, *apjl* **806**, L14 (2015).
- [27] M. Ruiz, R. N. Lang, V. Paschalidis, and S. L. Shapiro, *Astrophys. J.* **824**, L6 (2016).
- [28] K. Beckwith, J. F. Hawley, and J. H. Krolik, *Astrophys. J.* **678**, 1180 (2008).
- [29] Z. B. Etienne, V. Paschalidis, and S. L. Shapiro, *prd* **86**, 084026 (2012).
- [30] E. Berger, *Ann. Rev. Astron. Astroph.* **52**, 43 (2014).
- [31] K. Kiuchi, K. Kyutoku, Y. Sekiguchi, M. Shibata, and T. Wada, *Phys.Rev.* **D90**, 041502 (2014).
- [32] K. Kiuchi, P. Cerd-Durn, K. Kyutoku, Y. Sekiguchi, and M. Shibata, *Phys. Rev.* **D92**, 124034 (2015).
- [33] D. A. Kann *et al.*, *Astrophys. J.* **734**, 96 (2011).
- [34] K. Hotokezaka, K. Kiuchi, K. Kyutoku, H. Okawa, Y.-i. Sekiguchi, M. Shibata, and K. Taniguchi, *Phys. Rev. D* **87**, 024001 (2013).
- [35] C. Palenzuela, S. L. Liebling, D. Neilsen, L. Lehner, O. L. Caballero, E. O'Connor, and M. Anderson, *Phys. Rev.* **D92**, 044045 (2015).
- [36] R. Ciolfi, W. Kastaun, B. Giacomazzo, A. Endrizzi, D. M. Siegel, and R. Perna, *Phys. Rev.* **D95**, 063016 (2017), arXiv:1701.08738 [astro-ph.HE].
- [37] Y. Sekiguchi, K. Kiuchi, K. Kyutoku, and M. Shibata, *prd* **91**, 064059 (2015).
- [38] F. Foucart, E. O'Connor, L. Roberts, L. E. Kidder, H. P. Pfeiffer, and M. A. Scheel, *Phys. Rev.* **D94**, 123016 (2016).
- [39] L. Lehner, S. L. Liebling, C. Palenzuela, O. L. Caballero, E. O'Connor, M. Anderson, and D. Neilsen, *Class. Quant. Grav.* **33**, 184002 (2016).
- [40] M. Shibata and K. Uryu, *Prog. Theor. Phys.* **107**, 265 (2002).
- [41] M. Shibata, K. Taniguchi, and K. Uryū, *Phys. Rev. D* **68**, 084020 (2003).
- [42] M. Shibata and K. Taniguchi, *Phys. Rev. D* **73**, 064027 (2006).
- [43] M. Shibata and K. Taniguchi, *Phys. Rev.* **D73**, 064027 (2006).
- [44] L. Rezzolla, L. Baiotti, B. Giacomazzo, D. Link, and J. A. Font, *Microphysics in computational relativistic astrophysics. Proceedings, Workshop, MICRA2009, Copenhagen, Denmark, August 24-28, 2009*, *Class. Quant. Grav.* **27**, 114105 (2010).
- [45] T. Kawamura, B. Giacomazzo, W. Kastaun, R. Ciolfi, A. Endrizzi, L. Baiotti, and R. Perna, *Phys. Rev.* **D94**, 064012 (2016), arXiv:1607.01791 [astro-ph.HE].
- [46] O. Just, M. Obergaulinger, H. T. Janka, A. Bauswein, and N. Schwarz, *Astrophys. J.* **816**, L30 (2016).
- [47] A. Perego, H. Yasin, and A. Arcones, (2017), arXiv:1701.02017 [astro-ph.HE].
- [48] Y. T. Liu, S. L. Shapiro, Z. B. Etienne, and K. Taniguchi, *Phys. Rev.* **D78**, 024012 (2008).
- [49] M. D. Duez, *Classical and Quantum Gravity* **27**, 114002 (2010).
- [50] M. Shibata, K. Taniguchi, and K. Uryu, *Phys. Rev.* **D71**, 084021 (2005).
- [51] C. Cutler and E. E. Flanagan, *Phys. Rev.* **D49**, 2658 (1994).
- [52] B. S. Sathyaprakash and B. F. Schutz, *Living Rev. Rel.* **12**, 2 (2009).
- [53] A. Maselli, L. Gualtieri, and V. Ferrari, (2013).
- [54] T. Hinderer, B. D. Lackey, R. N. Lang, and J. S. Read, *Phys. Rev.* **D81**, 123016 (2010).
- [55] T. W. Baumgarte, S. L. Shapiro, and M. Shibata, *apjl* **528**, L29 (2000), astro-ph/9910565.
- [56] Z. B. Etienne, J. A. Faber, Y. T. Liu, S. L. Shapiro, K. Taniguchi, *et al.*, *Phys.Rev.* **D77**, 084002 (2008).
- [57] Z. B. Etienne, Y. T. Liu, V. Paschalidis, and S. L. Shapiro, *Phys.Rev.* **D85**, 064029 (2012).
- [58] Z. B. Etienne, V. Paschalidis, Y. T. Liu, and S. L. Shapiro, *Phys.Rev.* **D85**, 024013 (2012).
- [59] Z. B. Etienne, Y. T. Liu, and S. L. Shapiro, *Phys.Rev.* **D82**, 084031 (2010).
- [60] M. Shibata and T. Nakamura, *Phys. Rev. D* **52**, 5428 (1995).
- [61] T. W. Baumgarte and S. L. Shapiro, *prd* **59**, 024007 (1998).
- [62] C. Bona, J. Masso, E. Seidel, and J. Stela, *Phys. Rev. Lett.* **75**, 600 (1995).
- [63] M. Alcubierre, B. Bruegmann, P. Diener, M. Koppitz, D. Pollney, E. Seidel, and R. Takahashi, *Phys. Rev.* **D67**, 084023 (2003).
- [64] M. Ruiz, D. Hilditch, and S. Bernuzzi, *Phys. Rev.* **D83**, 024025 (2011).
- [65] K. Taniguchi and E.ourgoulhon, *Phys. Rev. D* **66**, 104019 (2002).
- [66] M. D. Duez, Y. T. Liu, S. L. Shapiro, and B. C. Stephens, *Phys.Rev.* **D72**, 024028 (2005).
- [67] B. D. Farris, R. Gold, V. Paschalidis, Z. B. Etienne, and S. L. Shapiro, *Phys.Rev.Lett.* **109**, 221102 (2012).
- [68] B. Giacomazzo, J. G. Baker, M. C. Miller, C. S. Reynolds, and J. R. van Meter, *Astrophys. J.* **752**, L15 (2012).
- [69] V. Paschalidis, Z. B. Etienne, and S. L. Shapiro, *Phys.Rev.* **D88**, 021504 (2013).
- [70] M. Bejger, D. Gondek-Rosinska, E.ourgoulhon, P. Haensel, K. Taniguchi, and J. L. Zdunik, *Astron. Astrophys.* **431**, 297 (2005).
- [71] J. Thornburg, *Class. Quant. Grav.* **21**, 743 (2004).
- [72] M. Alcubierre *et al.*, *Phys. Rev.* **D72**, 044004 (2005).
- [73] M. Ruiz, R. Takahashi, M. Alcubierre, and D. Nunez, *Gen. Rel. Grav.* **40**, 2467 (2008).
- [74] R. Gold, V. Paschalidis, Z. B. Etienne, S. L. Shapiro, and H. P. Pfeiffer, *Phys.Rev.* **D89**, 064060 (2014), arXiv:1312.0600 [astro-ph.HE].
- [75] M. D. Duez, Y. T. Liu, S. L. Shapiro, M. Shibata, and B. C. Stephens, *Phys. Rev. D* **73**, 104015 (2006).
- [76] S. L. Shapiro, *Astrophys.J.* **544**, 397 (2000).
- [77] N. D. Lyford, T. W. Baumgarte, and S. L. Shapiro, *Astrophys. J.* **583**, 410 (2003), gr-qc/0210012.
- [78] J. C. McKinney, *ArXiv Astrophysics e-prints* (2005), arXiv:astro-ph/0506368.
- [79] R. D. Blandford and R. L. Znajek, *mnras* **179**, 433 (1977).
- [80] B. D. Farris, Y. T. Liu, and S. L. Shapiro, *Phys.Rev.* **D81**, 084008 (2010).
- [81] C. F. Gammie and S. A. Balbus, *mnras* **270**, 138 (1994).
- [82] J. H. Krolik and J. F. Hawley, in *The Multicolored Landscape of Compact Objects and Their Explosive Origins Landscape of Compact Objects and Their Explosive Origins*, American Institute of Physics Conference Series, Vol. 924, edited by T. di Salvo, G. L. Israel, L. Piersant, L. Burderi, G. Matt, A. Tornambe, and M. T. Menna (2007) pp. 801–808, astro-ph/0611605.
- [83] R. Mochkovitch, M. Hernanz, J. Isern, and X. Martin, *Nature (London)* **361**, 236 (1993).
- [84] M. Shibata, K. Taniguchi, and K. Uryū, *prd* **71**, 084021 (2005).
- [85] A. Bauswein and N. Stergioulas, (2017), arXiv:1702.02567 [astro-ph.HE].